

The Hbot : A Holonomic Spherical Haptic Interface Driven by Non-Holonomic Wheels

Wisdom C. Agboh

Abstract—We present the Hbot, a holonomic, singularity-free spherical robot designed for haptic simulations. The Hbot is made up of a caged sphere actuated by steered and driven non-holonomic wheels to produce continuous and unlimited spherical motions. We analyse the kinematic interface between a sphere and n arbitrarily positioned, steered and driven non-holonomic wheels in the general case. We also present a detailed singularity analysis and show that workspace-boundary and workspace-interior singularities can both be avoided at the design stage. We implement a prototype using two steered and driven non-holonomic wheels and show experimental results for trajectory tracking and rendering of various rotational stiffness levels.

I. INTRODUCTION

Haptic devices are essential in our world today with applications ranging from surgery to search and rescue. They have become even more important for tasks where visual information alone is not sufficient and may result in undesired errors. A typical example is minimally invasive surgical training where haptic feedback has improved the training performance of surgeons [1]. Haptic devices can have different types of workspace requirements depending on the desired application. In this work, we are interested in the generation of continuous and unlimited spherical motions for haptic simulations.

A flight simulator [2] for example, requires a mechanism with unlimited spherical motions to achieve a meaningful performance. Moreover, in neuro-physiological experimental studies [3], a device with unlimited spherical motion is required to study the contribution of vision and proprioception to the perception and control of hand orientations in three-dimensional orientation-matching tasks. Currently, spherical motions are produced either by spherical motors or more general mechanisms.

Spherical motors in general, produce the desired unlimited spherical motions by utilizing electromagnetism or piezoelectricity. Kumagai et al. [4] and Kasashima et al. [5] both present electromagnetic motors which generally have a spherical rotor (made of a permanent magnet or a ferrous metal) and an electromagnetic stator. This arrangement yields the desired spherical motions through the generation of thrust forces on the rotor. These motors are generally complex in structure and have a slow response. On the other hand, piezoelectric spherical motors [6], [7] drive a spherical rotor with a traveling wave produced when voltage is applied to piezoelectric materials with different phases on the odd and even sets. Piezoelectric motors have a fast response with

no electromagnetic interference, but suffer from small power output and low efficiency [8].

Mechanisms that produce spherical motions can be grouped without loss of generality as gimbal-type, parallel-linkage type, devices that change a sphere's center of gravity, and sphere surface contact type devices. Osborne et al. [9] and Gao et al. [10] propose gimbal-type devices that generally possess a large workspace but are prone to the gimbal-lock and suffer from low stiffness and force output capacity. Parallel-linkage type devices [11], [12], and [13] feature high force bandwidths, low inertia, and passive back-driveability but have workspace boundary singularities and thus are unable to generate unlimited spherical motions. On the other hand, continuously changing the center of gravity of a sphere can result in unlimited spherical motions. Zhao et al. [14] and Gambari et al. [15] achieve this change in a sphere's center of gravity by controlling the pose of pendulums within the sphere. However, the resulting devices are relatively hard to control and complex in structure.

Furthermore, Ip et al. [16] propose a surface contact type device that uses a complex mechanism and magnets to apply surface-contact forces on a sphere. This device is able to generate unlimited spherical motions, however it strives to eliminate workspace boundary singularities through reconfigurable control which is prone to errors. The Atlas motion platform [17] is another surface-contact type device that uses three omni-directional special wheels to drive a sphere and generate singularity-free unlimited spherical motions. It is easy to control, but has sphere contact discontinuities, is relatively expensive and cannot be easily scaled up or down due to its special wheels.

In this paper, we present the Hbot, a novel three degrees of freedom (DOF) spherical parallel mechanism for haptic simulations. It is able to produce unlimited spherical motions without workspace boundary or interior singularities which can be avoided completely at the design stage. The Hbot uses at least two steered and driven non-holonomic wheels to produce holonomic and unlimited spherical motions. Moreover, using more than two wheels results in a redundant mechanism which presents several other advantages such as improved stability. The Hbot features a small footprint, high force bandwidths, high stiffness and passive back-drivability. In addition, since we use standard non-holonomic wheels, the Hbot has relatively better traction with continuous sphere-wheel contact. It is relatively cheaper and easily scalable. A special case of our device occurs when steered and driven conventional tyres are used to produce holonomic motions on a plane [18].

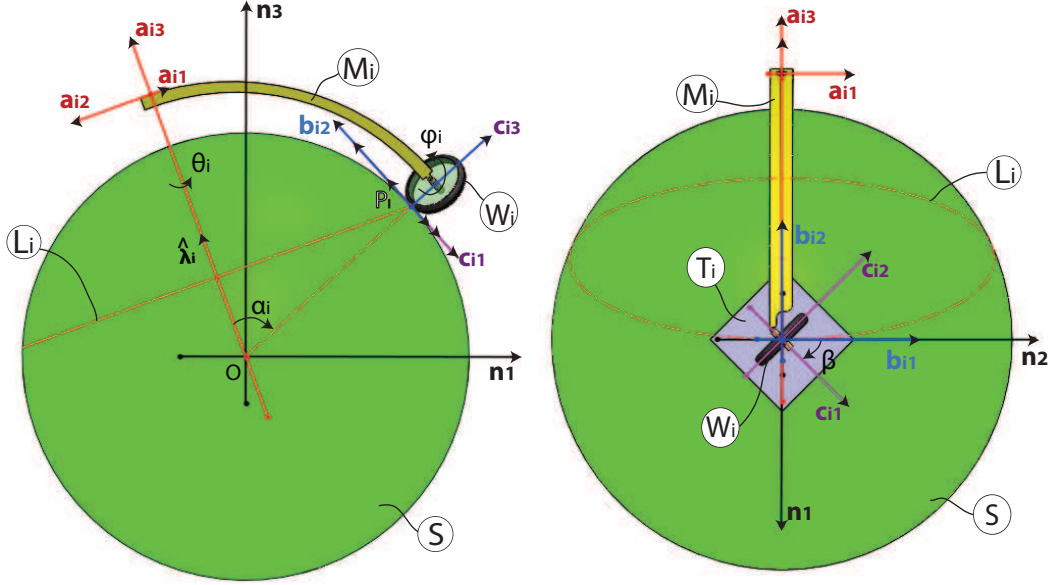


Figure 1: The relevant frames and points to define the kinematic interface between a sphere and arbitrary driven and steered non-holonomic wheels

We make the following contributions:

- We present the kinematic equations of motion for the kinematic interface between a sphere and n arbitrarily positioned, steered and driven non-holonomic wheels.
- We conduct a general singularity analysis of this mechanism and show that workspace-boundary and workspace-interior singularities can be avoided at the design stage.
- We implement a physical prototype of a spherical haptic interface with two steered and driven non-holonomic wheels.
- We analyse the Hbot in terms of its kinematic and dynamic performance.
- We evaluate the performance of the Hbot for rotational stiffness rendering and trajectory tracking.

Notation - Throughout this paper, angles are represented using Greek letters, vectors are in bold face, a hat denotes a unit vector, ${}^N R^W$ denotes the rotation matrix of frame W with respect to frame N , \mathbf{r}^{OP} denotes the position vector from point O to point P , ${}^N \mathbf{v}^P$ represents the velocity of point P with respect to frame N , ${}^N \omega^W$ represents the angular velocity of frame W with respect to frame N , and $\frac{d}{dt}(\mathbf{v})$ denotes the time derivative of vector \mathbf{v} in frame N .

The rest of the paper is organized as follows; in section II, the kinematic analysis for the generalized problem is presented, in section III, the detailed singularity analysis is shown. Furthermore, in section IV, we describe an implementation of the proposed device and in section V, we conduct kinematic and dynamic performance evaluation for the prototype. Section VI details results for trajectory tracking and impedance control using the prototype and section VII then concludes the paper.

II. KINEMATIC ANALYSIS

The generalized problem is that of a sphere actuated by driven and steered standard wheels positioned at n arbitrary

contact points with arbitrary orientations. The kinematics problem then becomes finding a geometrically feasible configuration for the wheels such that there is no kinematic slip between the standard wheels and the sphere. In Fig. 1, we define the inertial frame N to be at the center O of the sphere with radius R . Point p_i is the contact point between a standard wheel of radius r_i and the sphere where the subscript i denotes a specific standard wheel, T_i is the tangent plane to the sphere at p_i . We then write the rotation matrix ${}^N R^{W_i}$ of the wheel frame with respect to the inertial frame as;

$${}^N R^{W_i} = {}^N R^{A_i} \cdot A_i R^{B_i} \cdot B_i R^{C_i} \cdot C_i R^{W_i} \quad (1)$$

Where A_i , B_i , and C_i are auxiliary frames required to define a set of simple rotations between the inertial frame and the wheel frame. $\hat{\lambda}_i$ is an arbitrary unit vector representing the steering axis of an arbitrary wheel, θ_i is the steering angle of the wheel connected to the link M_i , α_i is the cone angle which defines the plane containing circle L_i on which point p_i lies, and ϕ_i defines the driving angle of the wheel. ${}^N R^{A_i}$ is defined as a rotation about axis $\hat{\lambda}_i$ by an amount of θ_i . It can be obtained by using Euler parameters. Given that the unit vector $\hat{\lambda}_i$ can be expressed as $\hat{\lambda}_i = \lambda_{i1} \mathbf{n}_1 + \lambda_{i2} \mathbf{n}_2 + \lambda_{i3} \mathbf{n}_3$, one can then obtain the relevant Euler parameters.

$A_i R^{B_i}$ is the rotation matrix between auxiliary frames B_i and A_i defined as a rotation about \mathbf{a}_1 (or \mathbf{b}_1) by a constant cone angle α_i , $B_i R^{C_i}$ is the rotation matrix between auxiliary frames C_i and B_i defined as a rotation about axis \mathbf{b}_3 (or \mathbf{c}_3) by an amount of a constant angle β_i , and $C_i R^{W_i}$ is the rotation matrix between the auxiliary frame C_i and the wheel frame W_i defined as a rotation about the driving axis \mathbf{w}_1 (or \mathbf{c}_1) with an amount of ϕ_i . Having defined the relationship between the relevant frames, one can then write the non-holonomic constraint equations for an arbitrary wheel in contact with a sphere at a single point as;

$$({}^N \mathbf{v}^{P_{iw}} - {}^N \mathbf{v}^{P_{is}}) \cdot \mathbf{c}_{i1} = 0 \quad (2)$$

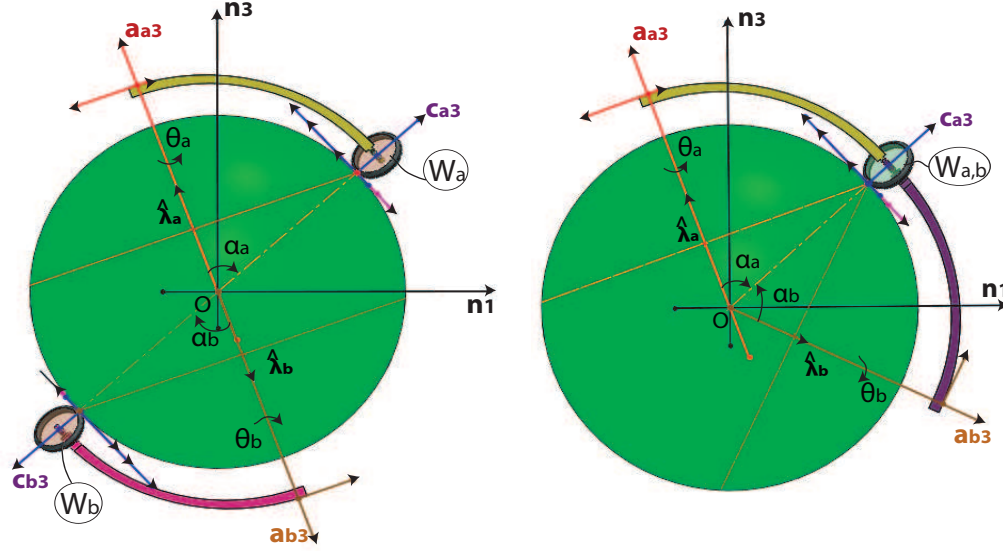


Figure 3: Workspace-interior singularity configurations

constraint equation describing the kinematic interface between a sphere and n arbitrary steered and driven wheels. Workspace interior singularities occur when Z is not full rank while workspace boundary singularities occur when H is singular.

A. Workspace Boundary Singularities

Workspace boundary singularities are based on matrix H which is a $2n \times 2n$ block diagonal matrix in the general case of n wheels. Since H is diagonal, its determinant is the product of the determinants of H_i corresponding to each wheel i ;

$$\det(H) = \det(H_1) \det(H_2) \dots \det(H_{n-1}) \det(H_n) \quad (14)$$

The determinant of H_i for each wheel can be found as;

$$\det(H_i) = rR(\hat{\lambda}_i \cdot \mathbf{c}_{i2}) \quad (15)$$

Eq. 15 should then be set to zero to find the relevant singularity conditions. Given that r and R are non-zero for a realistic implementation, it then follows that $\hat{\lambda}_i \cdot \mathbf{c}_{i2} = 0$ is the required condition that yields workspace boundary singularities. A physical interpretation of this result states that workspace boundary singularities occur when the steering axis $\hat{\lambda}_i$ and the driving axis \mathbf{c}_{i1} are aligned for a wheel such that velocities produced by steering the wheel and those produced by driving the wheel are linearly dependent. This singularity configuration is depicted in Fig 2 and can clearly be avoided at the design stage of a physical prototype.

B. Workspace Interior Singularities

Workspace interior singularities are based on matrix Z which is a $2n \times 3$ matrix in the general case of n wheels. Notice that Z_i is full rank in the case of only one wheel. This is clearly as a result of the fact that $C_i R^N$ is a rotation matrix whose determinant is unity, and the matrix multiplying $C_i R^N$ has linearly independent rows and columns. However, for two wheels (A & B), the matrix Z is expressed as:

$$Z = -R \begin{bmatrix} 0 & 1 & 0 \\ -1 & 0 & 0 \\ 0 & 1 & 0 \\ -1 & 0 & 0 \end{bmatrix} \begin{bmatrix} C_A R^N \\ C_B R^N \end{bmatrix} \quad (16)$$

Clearly, for this case the matrix Z loses rank only when $C_A R^N = C_B R^N$. This implies that workspace interior singularities for the two-wheel case occur when the wheels are at the same orientation with respect to the sphere. Meaning that they are either collocated or one wheel is located at the antipodal point of the other wheel on the sphere. Fig. 3 shows the workspace interior singularity configurations for two wheels.

Intuitively, these singular configurations occur when the steering and driving velocities of one wheel are linearly dependent on those of another wheel. It is obvious that just like the workspace-boundary singularities, workspace-interior singular configurations can also be avoided at the design stage.

In order to fully control the orientation of the sphere in the manifold $SO(3)$, one requires at least two active wheels. Therefore, in the case of n -wheels ($n \geq 2$), driving a sphere, it is sufficient to ensure that there exist at least a pair of wheels that produce linearly independent steering and driving velocities in order to avoid workspace interior singularities. Taking into consideration the fact that the proposed device can produce unlimited spherical motions, it follows that the singularity-free workspace covers the manifold $SO(3)$.

IV. IMPLEMENTATION AND CHARACTERIZATION

A. Physical Implementation

A prototype of the spherical robot is designed using two wheels A and B as shown in Fig. 4. A ball-bearing cage is used to ensure proper sphere centering and to carry the weight of the end-effector which is a hollow plastic sphere of mass 467 g and radius 102 mm. An important part of the design is the avoidance of singularities within the spherical

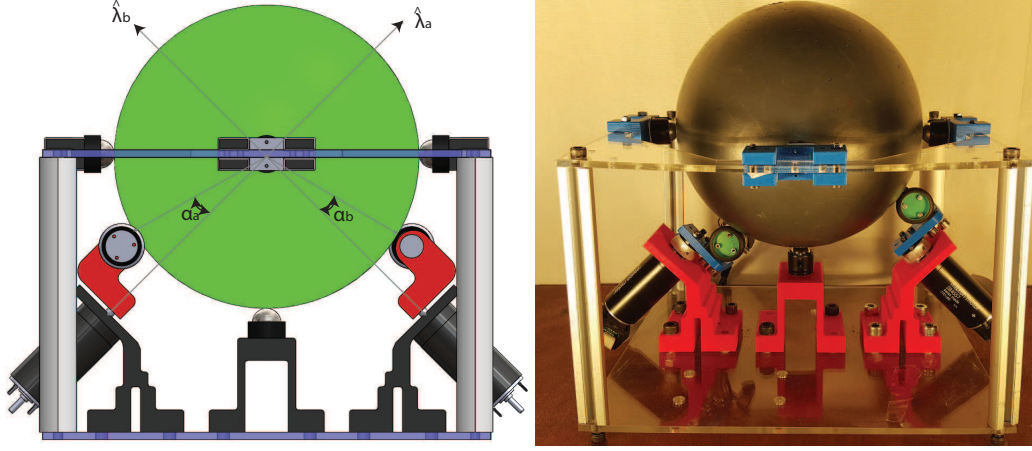


Figure 4: 3D CAD rendering (left) and prototype (right)

unlimited workspace. Workspace boundary singularities are avoided by ensuring that the steering axis and the driving axis never become parallel for any given wheel. Workspace interior singularities are avoided by ensuring that the wheels can never collocated on the sphere such that they can always generate linearly independent steering and driving velocities. A singularity-free workspace is then achieved by selecting the design parameters as shown in Table I for the prototype herein.

Table I: Design Parameters for the Prototype

Parameter	Wheel A	Wheel B
$\alpha(\text{radians})$	0.1745	0.1745
$\beta(\text{radians})$	0	0
$\hat{\lambda}$	$0.7071 \mathbf{n}_1 - 0.7071 \mathbf{n}_3$	$-0.7071 \mathbf{n}_1 - 0.7071 \mathbf{n}_3$

Notice that the upper half of the prototype is left open by design to facilitate better interactions with the spherical end-effector. Furthermore, low-inertia direct drive actuators are used for the grounded motors which are 90 *Watt* brushed motors while the actuators on the rotating links are low-weight (24 *g*) 3 *Watt* motors with 17:1 gear reduction ratio. This specific selection of the actuators results in a prototype that both has a low apparent end-effector inertia and is passively backdriveable.

B. Experimental Characterization

The bandwidth is an important property of force-feedback devices. The Hbot is a parallel mechanism with low-apparent inertia and direct drive actuation hence a high bandwidth is expected. Under closed loop orientation control, Fig. 5 is experimentally obtained and a bandwidth of 5.50 Hz can be observed. Furthermore, since safety during operation is always important, the Hbot, a force-feedback device should be passively back-driveable. This problem is tackled at the design stage with the selection of direct drive actuators. We then verify passive backdriveability by measuring the minimum torque required to induce motion along the degrees of freedom of the device. Our results show that minimum torques of 5

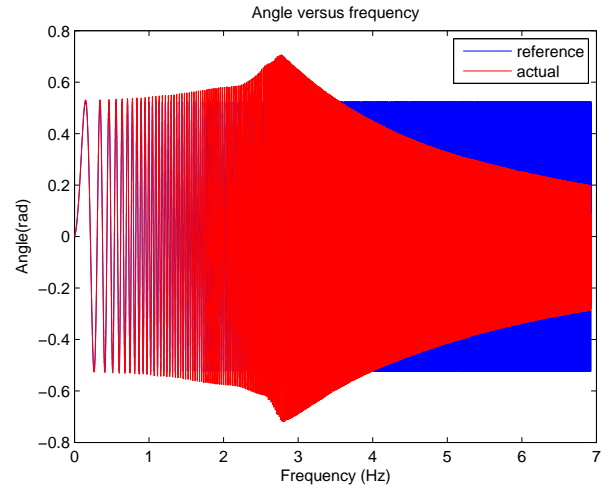


Figure 5: Angle versus frequency plot under closed loop position control

mNm, 4 mNm, and 4 mNm are required to induce visible rotations about \mathbf{n}_1 , \mathbf{n}_2 and \mathbf{n}_3 respectively.

Torques generated by the Hbot are expected to cover torque limits for specific haptic applications. The maximum instantaneous and continuous torques generated by the motors are $[0.14, 0.93, 0.93]$ Nm and $[0.023, 0.073, 0.073]$ Nm respectively and when mapped to the end-effector, they become $[1.4, 0.94, 0.84]$ Nm and $[0.11, 0.15, 0.065]$ Nm respectively. In Table II, we summarize results of our experimental characterization.

Table II: Experimental Characterization of the Hbot

Criterion	\mathbf{n}_1	\mathbf{n}_2	\mathbf{n}_3
Peak Inst. Torque[Nm]	1.4	0.94	0.84
Peak Cont. Torque[Nm]	0.11	0.15	0.065
Back-driveability [Nm]	5×10^{-3}	4×10^{-3}	4×10^{-3}
Position Bandwidth [Hz]	5.50	5.50	5.50

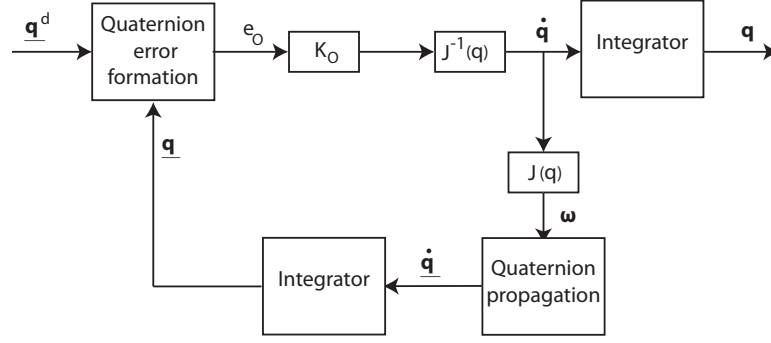


Figure 6: Inverse kinematics control to obtain joint variables at sampled points in $SO(3)$

V. KINEMATIC AND DYNAMIC PERFORMANCE

Here, we investigate the kinematic/dynamic performance of our prototype. Performance measures are generally required for the design, task planning and synthesis of manipulators. Optimal task-specific mechanism structures are obtained based on optimizing the desired performance metric. There are numerous measures of performance that exist in the literature which can be classified as kinematic/dynamic or local/global without loss of generality.

A. Kinematic Performance

Kinematic performance metrics are based on the Jacobian matrix. They include but are not limited to the kinematic manipulability index [19] and the condition number [20] which are local indices (configuration dependent) but can be integrated over the mechanism's workspace to generate global performance measures. The condition number has been proven to be a better measure of the degree of ill-conditioning of a mechanism than the manipulability index and hence the condition number which is an unbounded measure is adopted here. It is given as ;

$$\kappa = \|J\| \|J^{-1}\| \quad (17)$$

Where J is the kinematic Jacobian and $\|\cdot\|$ denotes a frame-invariant norm given as;

$$\|J\| = \sqrt{\text{tr}(JWJ^T)}$$

with $W = (1/n)I$, where I is the identity matrix and n is the dimension of the Jacobian matrix. However, κ is unbounded and can result in computational problems. The reciprocal of κ - the local conditioning index, $LCI \in [0, 1]$ is then selected ;

$$LCI = \frac{1}{\kappa} \quad (18)$$

A corresponding global performance measure - the global conditioning index, GCI [21] demonstrating the distribution of the conditioning number over the entire workspace is adopted and is given as;

$$GCI = \frac{1}{n_W} \sum_{j=1}^{n_W} \frac{1}{\kappa} \quad (19)$$

where n_W are workspace nodes of the mechanism.

B. Dynamic Performance

Dynamic performance metrics are based on the inertia matrix which is obtained here by Lagrange's formulation. A widely used measure - the dynamic manipulability index, μ_d estimates the ability of a mechanism to generate acceleration based on a driving force at the joints and is selected here. It is given for non-redundant manipulators [22] as;

$$\mu_d = \left| \frac{\det(J)}{\det(M)} \right| \quad (20)$$

where M is the inertia matrix. However, μ_d is unbounded so the normalized manipulability index is selected and given as;

$$\mu = \frac{\mu_i}{\mu_{max}} \quad (21)$$

where μ_i is the manipulability index at a given point and μ_{max} is the maximum manipulability index in the entire workspace. μ is then integrated over the entire workspace to generate the global manipulability index, GMI as follows;

$$GMI = \frac{1}{n_W} \sum_{j=1}^{n_W} \mu \quad (22)$$

where n_W are workspace nodes of the mechanism.

C. Uniform Sampling of $SO(3)$

To calculate the performance measures enlisted in the preceding sections, knowledge of the mechanism's workspace is paramount. The workspace in question is the 3D rotation group $SO(3)$, and a uniform set of points within the workspace should be generated in order to ensure that the global performance metrics are calculated from evenly distributed sampled data points. Yershova et al. [23], use Hopf coordinates (θ, ϕ, ψ) to generate quaternions that parametrize $SO(3)$. Each quaternion, \underline{q} can be written as a function of the Hopf coordinates as follows:

$$\begin{aligned} q_0 &= \cos(\theta/2) \cos(\psi/2) \\ q_1 &= \cos(\theta/2) \sin(\psi/2) \\ q_2 &= \sin(\theta/2) \cos(\phi + \psi/2) \\ q_3 &= \sin(\theta/2) \sin(\phi + \psi/2) \end{aligned} \quad (23)$$

where θ, ϕ, ψ have ranges of $\pi, 2\pi, 2\pi$ respectively. A set of uniformly sampled points in $SO(3)$ is then generated by varying each coordinate between its limits with a specified step size h .

D. Inverse Kinematics Control and Performance Results

Upon generating the uniformly sampled set of orientations in the workspace, a set of joint variables corresponding to those points is then sought in order to calculate the desired metrics. Obtaining these points is however not straightforward because of the non-holonomic relationship between the end-effector pose and joint variables. Inverse kinematics control shown in Fig. 6 is then proposed to take the end-effector in simulation, from a fixed initial orientation to each of the sampled orientations on $SO(3)$ such that the corresponding joint variables at those sampled points are calculated. In this control architecture, \mathbf{q}^d is the desired sampled orientation and \mathbf{q} is the corresponding calculated joint variable vector. K_O is the control gain usually selected as a diagonal matrix. The quaternion error is formed from $\mathbf{q}^d = (\eta_d, \epsilon_d)$ and $\mathbf{q} = (\eta, \epsilon)$ as follows;

$$e_O = \eta \epsilon_d - \eta_d \epsilon - S(\epsilon_d) \epsilon \quad (24)$$

With this control scheme, results show RMS tracking error \mathbf{e}_O of $[0.0354, 0.0368, 0.0312]^T$ rad, and percent RMS value with respect to the maximum position of $[3.54\%, 3.68\%, 3.12\%]^T$. The performance metrics are then computed since both the sampled orientation in $SO(3)$ and the corresponding joint variable vector are now available. The GCI was found to be 0.41 while the normalized GMI was found as 0.5. These values indicate an average performance for the Hbot. However, one can find design parameters that optimize a desired performance metric.

VI. IMPEDANCE CONTROL IN $SO(3)$ AND EXPERIMENTAL EVALUATION

Impedance control is a well-established control strategy for the interactions between a robot's end-effector and the environment. Modeling the prototype as an impedance-type device, open-loop impedance control is then an appropriate strategy for trajectory tracking and virtual stiffness rendering. In the task space, minimal representations are typically used to represent the orientation of the end-effector and this leads to representation singularities. Moreover, this minimal representation does not hold a physical meaning considering the definition of an end-effector's rotational impedance.

Caccavale et al. [24], propose proper global representations to define the rotational impedance of a robot's end-effector. Specifically, using unit quaternions $\mathbf{q}_a = (\eta_a, \epsilon_a)$ and $\mathbf{q}_d = (\eta_d, \epsilon_d)$ to represent the orientation of the actual and desired end-effector frames respectively, the impedance equation can be written as:

$$M_o (\dot{\mathbf{N}}\omega^d - \dot{\mathbf{N}}\omega^a) + D_o (\mathbf{N}\omega^d - \mathbf{N}\omega^a) + K_o \epsilon_{da} = T \quad (25)$$

Where $\mathbf{N}\omega^d$ and $\mathbf{N}\omega^a$ are the angular velocities of the desired and actual frames with respect to the inertial frames respectively, T is the contact moment at the end-effector, M_o , D_o , and K_o are positive definite matrices describing the generalized inertia, rotational damping and rotational stiffness respectively. K_o is expressed as;

$$K_o = 2E^T K \quad (26)$$

Where,

$$E = \eta_{da} I - S(\epsilon_{da}) \quad (27)$$

$$\eta_{da} = \eta_d \eta_a + \epsilon_d^T \epsilon_a \quad (28)$$

$$\epsilon_{da} = \eta_d \epsilon_a - \eta_a \epsilon_d - S(\epsilon_d) \epsilon_a \quad (29)$$

and $S(\cdot)$ is the skew symmetric operator. To evaluate the trajectory tracking performance of the prototype, a chirp orientation signal with a 35 degree amplitude and frequencies increasing up to 1 Hz is applied as the reference orientation trajectory. This signal is applied along n_1 rotational axis and Fig. 7 shows the chirp signal tracking performance along this axis. The RMS trajectory tracking error is calculated to be 1% when the errors are generated at the joints. However, this is not realistic as problems such as slip, stiction, improper centering tend to increase tracking errors for the prototype. Thus, an external error measurement system is required. Here an external camera is used to track the orientation of the end-effector by aligning the axis of rotation with the axis of the camera such that the tracked point is sure to follow a circular path on a plane. Fig. 7 also shows the results obtained from the external tracking system where the RMS tracking error was found to be less than 8%. Furthermore,

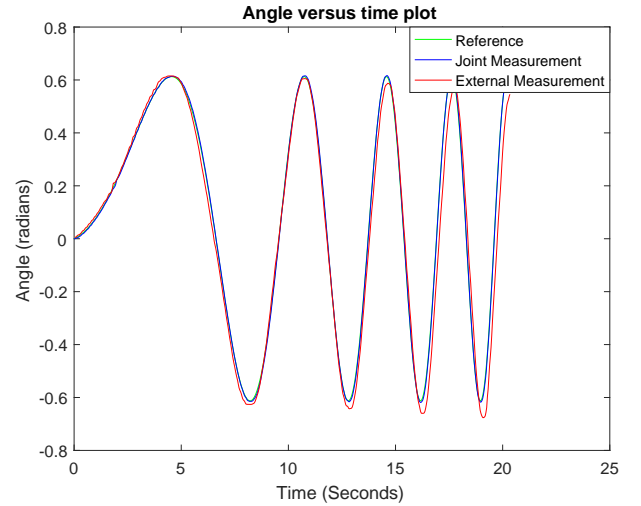


Figure 7: Trajectory tracking about n_1 axis

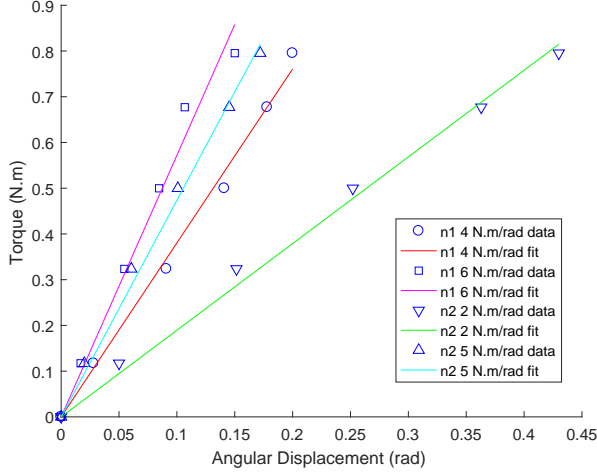
virtual rotational stiffness levels around 2 different axis have been rendered. Fig 8 presents torque-deflection data measured for these renderings after applying known torques to the sphere and measuring its deflection. Table III presents R^2 values characterizing the quality of the line fit, the slope of these lines, and the rendering error. The implication of this result is that even under open loop impedance control (without force feedback), high fidelity impedance renderings with RMS errors less than 5.5% can be achieved with the device. A video of the prototype can be found at https://youtu.be/R8WMv_JpUM

VII. CONCLUSION AND FUTURE WORK

In this paper, we presented the kinematics, singularity analysis, functional prototype and real-time impedance control of the Hbot - a novel 3 DoF spherical parallel mechanism. For

Table III: Spring rendering results for the device

Axis	Desired stiffness [N.m/rad]	Slope of fitted line [N.m/rad]	Rendering error [%]	Quality of fit (R^2)
\mathbf{n}_1	4.00	3.80	5.00	99.36
\mathbf{n}_1	6.00	5.72	4.67	98.13
\mathbf{n}_2	2.00	1.89	5.50	99.42
\mathbf{n}_2	5.00	4.74	5.2	99.42

Figure 8: Virtual rotational stiffness rendering about \mathbf{n}_1 and \mathbf{n}_2 directions

the first time, the general kinematics of a sphere actuated by steered and driven non-holonomic wheels has been explored. A major result obtained here is the fact that singularities can be avoided at the design stage. Workspace-boundary singularities are avoided by ensuring that the driving and steering axis of each wheel are never parallel while workspace-interior singularities are avoided by ensuring that for at least two wheels in the general case of n -wheels, the steering and driving velocities of one wheel are linearly independent of those of the other wheel.

Furthermore, the Hbot features parallel kinematics with analytical solutions and is modeled as an impedance-type device. As a result of its direct-drive and grounded actuation, open-loop impedance control results show the possibility of using the device for haptic simulations. It is noteworthy that proper end-effector (sphere) centering is crucial to achieve good results. Ongoing work include optimal dimensional synthesis of the device and experimental evaluation of its effectiveness in various applications from flight simulation to neurophysiology studies.

ACKNOWLEDGMENT

The author would like to thank Volkan Patoglu for very useful discussions.

REFERENCES

[1] P. Ström, L. Hedman, L. Särnå, A. Kjellin, T. Wredmark, and L. Felländer-Tsai, "Early exposure to haptic feedback enhances performance in surgical simulator training: a prospective randomized crossover study in surgical residents," *Surgical Endoscopy And Other Interventional Techniques*, vol. 20, no. 9, pp. 1383–1388, Sep 2006. [Online]. Available: <https://doi.org/10.1007/s00464-005-0545-3>

[2] B. Volkaner, S. N. Sozen, and V. E. Omurlu, "Realization of a desktop flight simulation system for motion-cueing studies," *International Journal of Advanced Robotic Systems*, vol. 13, no. 3, p. 85, 2016. [Online]. Available: <https://doi.org/10.5772/63239>

[3] N. Gosselin-Kessib, J. Messier, and J. F. Kalaska, "Evidence for automatic on-line adjustments of hand orientation during natural reaching movements to stationary targets," *Journal of Neurophysiology*, vol. 99, no. 4, pp. 1653–1671, 2008. [Online]. Available: <http://jn.physiology.org/content/99/4/1653>

[4] M. Kumagai and R. L. Hollis, "Development and control of a three dof spherical induction motor," in *2013 IEEE International Conference on Robotics and Automation*, May 2013, pp. 1528–1533.

[5] N. Kasashima, K. Ashida, T. Yano, A. Gofuku, and M. Shibata, "Torque control method of an electromagnetic spherical motor using torque map," *IEEE/ASME Transactions on Mechatronics*, vol. 21, no. 4, pp. 2050–2060, Aug 2016.

[6] X. Yang, Y. Liu, W. Chen, and J. Liu, "Sandwich-type multi-degree-of-freedom ultrasonic motor with hybrid excitation," *IEEE Access*, vol. 4, pp. 905–913, 2016.

[7] Y. Ting, Y. R. Tsai, B. K. Hou, S. C. Lin, and C. C. Lu, "Stator design of a new type of spherical piezoelectric motor," *IEEE Transactions on Ultrasonics, Ferroelectrics, and Frequency Control*, vol. 57, no. 10, pp. 2334–2342, October 2010.

[8] C. Zhao, *Ultrasonic motors: technologies and applications*. Springer Science & Business Media, 2011.

[9] J. Osborne, G. Hicks, and R. Fuentes, "Global analysis of the double-gimbal mechanism," *IEEE Control Systems*, vol. 28, no. 4, pp. 44–64, Aug 2008.

[10] P. Gao, K. Li, L. Wang, and J. Gao, "A self-calibration method for non-orthogonal angles of gimbals in tri-axis rotational inertial navigation system," *IEEE Sensors Journal*, vol. 16, no. 24, pp. 8998–9005, Dec 2016.

[11] C. M. Gosselin and J. F. Hamel, "The agile eye: a high-performance three-degree-of-freedom camera-orienting device," in *Proceedings of the 1994 IEEE International Conference on Robotics and Automation*, May 1994, pp. 781–786 vol.1.

[12] A. Gupta, M. K. O'Malley, V. Patoglu, and C. Bugar, "Design, control and performance of ricewrist: A force feedback wrist exoskeleton for rehabilitation and training," *The International Journal of Robotics Research*, vol. 27, no. 2, pp. 233–251, 2008. [Online]. Available: <http://dx.doi.org/10.1177/0278364907084261>

[13] W. C. Agboh, M. Yalcin, and V. Patoglu, "A six degrees of freedom haptic interface for laparoscopic training," in *2016 IEEE/RSJ International Conference on Intelligent Robots and Systems (IROS)*, Oct 2016, pp. 1107–1112.

[14] B. Zhao, M. Li, H. Yu, H. Hu, and L. Sun, "Dynamics and motion control of a two pendulums driven spherical robot," in *2010 IEEE/RSJ International Conference on Intelligent Robots and Systems*, Oct 2010, pp. 147–153.

[15] A. Ghanbari, S. Mahboubi, and M. M. S. Fakhraabadi, "Design, dynamic modeling and simulation of a spherical mobile robot with a novel motion mechanism," in *Proceedings of 2010 IEEE/ASME International Conference on Mechatronic and Embedded Systems and Applications*, July 2010, pp. 434–439.

[16] S. H. Ip, C. Chen, R. P. H. Chen, and D. Oetomo, "Development of reconfigurable spherical motion generator," in *Advances in Reconfigurable Mechanisms and Robots I*, J. S. Dai, M. Zoppi, and X. Kong, Eds. London: Springer London, 2012, pp. 285–293.

[17] A. Weiss, R. Langlois, and M. Hayes, "Unified treatment of the kinematic interface between a sphere and omnidirectional wheel actuators," *Journal of Mechanisms and Robotics*, vol. 3, no. 4, p. 041001, 2011.

[18] M. Wada and S. Mori, "Holonomic and omnidirectional vehicle with conventional tires," in *Robotics and Automation, 1996. Proceedings., 1996 IEEE International Conference on*, vol. 4. IEEE, 1996, pp. 3671–3676.

[19] T. Yoshikawa, "Manipulability of robotic mechanisms," *The International Journal of Robotics Research*, vol. 4, no. 2, pp. 3–9, 1985. [Online]. Available: <http://dx.doi.org/10.1177/027836498500400201>

[20] J. K. Salisbury and J. J. Craig, "Articulated hands," *The International Journal of Robotics Research*, vol. 1, no. 1, pp. 4–17, 1982. [Online]. Available: <http://dx.doi.org/10.1177/027836498200100102>

[21] C. Gosselin and J. Angeles, "A global performance index for the kinematic optimization of robotic manipulators," *Journal of Mechanical Design*, vol. 113, no. 3, pp. 220–226, September 1991.

[22] T. Yoshikawa, "Dynamic manipulability of robot manipulators," in *Proceedings. 1985 IEEE International Conference on Robotics and Automation*, vol. 2, Mar 1985, pp. 1033–1038.

- [23] A. Yershova, S. Jain, S. M. LaValle, and J. C. Mitchell, "Generating uniform incremental grids on $so(3)$ using the hopf fibration," *The International Journal of Robotics Research*, vol. 29, no. 7, pp. 801–812, 2010. [Online]. Available: <http://dx.doi.org/10.1177/0278364909352700>
- [24] F. Caccavale, C. Natale, B. Siciliano, and L. Villani, "Six-dof impedance control based on angle/axis representations," *IEEE Transactions on Robotics and Automation*, vol. 15, no. 2, pp. 289–300, Apr 1999.